NANO LETTERS

pubs.acs.org/NanoLett

Letter

Doping-Induced Superconductivity in the van der Waals Superatomic Crystal $Re_6Se_8Cl_2$

Evan J. Telford,[▽] Jake C. Russell,[▽] Joshua R. Swann, Brandon Fowler, Xiaoman Wang, Kihong Lee, Amirali Zangiabadi, Kenji Watanabe, Takashi Taniguchi, Colin Nuckolls, Patrick Batail, Xiaoyang Zhu, Jonathan A. Malen, Cory R. Dean,* and Xavier Roy*

Cite This: *Nano Lett.* 2020, 20, 1718–1724

Read Online

ACCESS | Metrics & More | Article Recommendations | Supporting Information

ABSTRACT: Superatomic crystals are composed of discrete modular clusters that emulate the role of atoms in traditional atomic solids. Owing to their unique hierarchical structures, these materials are promising candidates to host exotic phenomena, such as doping-induced superconductivity and magnetism. Low-dimensional superatomic crystals in particular hold great potential as electronic components in nanocircuits, but the impact of doping in such compounds remains unexplored. Here we report the electrical transport properties of $Re_6Se_8Cl_2$, a two-dimensional superatomic semiconductor. We find that this compound can be n-doped *in situ* through Cl dissociation, drastically altering the transport behavior from semiconducting to metallic and giving rise to superconductivity with a critical temperature of ~8 K and upper critical field exceeding 30 T. This work is the first example of superconductivity in a van der Waals superatomic crystal; more broadly, it establishes a new chemical strategy to manipulate the electronic properties of van der Waals materials with labile ligands.

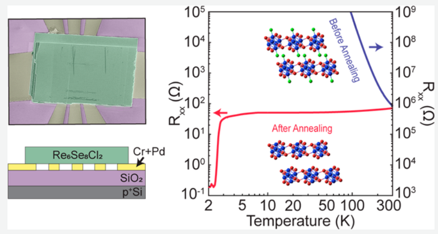

KEYWORDS: *superatomic, Chevrel phase, van der Waals, two-dimensional, semiconductor, current annealing, doping, superconductor*

Superatomic crystals have generated significant interest in materials science due to their modular and hierarchical structures, which allow for the design of electronically and chemically diverse materials.[1−11] Recently, layered van der Waals (vdW) superatomic crystals have been used to create a new family of hierarchical two-dimensional (2D) materials.[5,12−14] These compounds consist of clusters covalently linked in-plane with weak vdW interactions between the layers. Analogous to atomic vdW crystals such as graphene, BN, and transition metal dichalcogenides (TMDs),[15,16] these superatomic vdW crystals can be exfoliated to yield monolayer-thick 2D sheets but with the added ability to undergo chemical modification at any stage of preparation, including after exfoliation or even device fabrication.[5] Superatomic vdW crystals therefore offer to vastly expand the properties and functionalities available in 2D materials[17] and in structures with dynamic, on-demand tunability.

The superatomic vdW compound $Re_6Se_8Cl_2$ is a 2D structural analogue of the Chevrel phase class of materials, $M_xMo_6E_8$ (M = metal, E = S, Se, Te).[18−20] Like the Chevrel phase, $Re_6Se_8Cl_2$ consists of an octahedral metal cluster core (Re) with each face capped by a chalcogen atom (Se). In contrast to the Chevrel phase, however, each cluster is also capped with two apical Cl atoms, which facilitate vdW stacking of the covalently bound sheets (Figure 1A). The Re_6Se_8 core has been studied extensively as an isolated molecular unit[21] but until recently little was known about the electronic properties of $Re_6Se_8Cl_2$ crystals, save for its semiconducting nature at room temperature[22] with a wide electronic band gap (1.58 eV).[12]

Chen et al. recently established that in Chevrel phase compounds superconductivity arises from electron−phonon interactions, and that Peierls (intermolecular) modes are the most important contributors to this phenomenon.[23] In practice, superconductivity emerges when cations are inserted into the structure to modulate the number of electrons per cluster.[24−26] Given these results, could doping also reveal superconductivity in the two-dimensional Chevrel phase analogues? A significant challenge to answering this question is the lack of a synthetic strategy to dope such materials.

In this work, we show that predefined regions of thin $Re_6Se_8Cl_2$ flakes integrated into mesoscopic electrical devices can be doped with electrons by applying a novel *in situ* current annealing technique. In these regions, the carrier density is increased by 4−5 orders of magnitude and the material undergoes a semiconductor-to-superconductor transition with a superconducting critical temperature of ~8 K and critical field exceeding 30 T. Structural and chemical analyses indicate

Received: November 25, 2019
Revised: January 11, 2020
Published: February 17, 2020

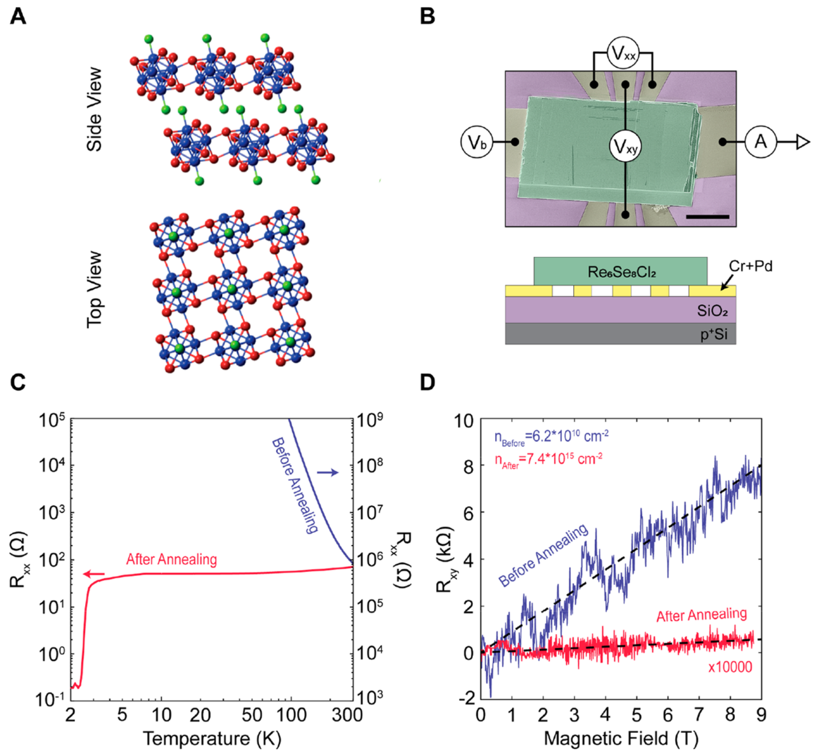

Figure 1. Electrical transport properties of $Re_6Se_8Cl_2$. (A) Crystal structure of $Re_6Se_8Cl_2$. Color code: Re, blue; Se, red; Cl, green. (B) Top: SEM image of a prepatterned transport device. The scale bar is 5 μm. The image is false colored so that the $Re_6Se_8Cl_2$ flake, prepatterned Pd electrodes, and SiO_2 substrate appear green, yellow, and purple, respectively. The measurement scheme is overlaid. Bottom: Side view of the device architecture. (C) R_{xx} versus temperature before (blue) and after (red) current annealing. (D) Antisymmetrized R_{xy} before (blue, measured at 200 K) and after (red, measured at 10 K) current annealing. Electronic carrier density per layer is extracted using the Hall coefficient $n_{3D} \times t = n_{2D} = \frac{B}{eR_{xy}}$. $\frac{R_{xy}}{B}$ is determined by fitting the data in (C) to a line (dashed black lines).

that the current bias-induced doping of $Re_6Se_8Cl_2$ results from the dissociation of Cl atoms.[12] The robustness of the superconducting state to out-of-plane magnetic fields exceeds known vdW superconductors, such as transition metal dichalcogenides[27,28] and twisted bilayer graphene,[29] while remaining air stable and retaining its properties over multiple cooldowns and after long time exposure to ambient lab conditions. This suggests significantly more favorable characteristics for technological applications.

Figure 1B shows a scanning electron microscopy image of an electrical transport device. We use a prepatterned lead geometry to electrically contact mechanically exfoliated $Re_6Se_8Cl_2$ flakes (thickness ~100−600 nm), allowing for simultaneous 4-terminal longitudinal (R_{xx}) and Hall resistance (R_{xy}) measurements (see Supporting Information for fabrication details). The $Re_6Se_8Cl_2$ flakes exhibit semiconducting behavior with the resistance strongly increasing with decreasing temperature (Figure 1C). Fitting to a thermally activated model, $R_{xx} = R_0 e^{(E_C - E_F)/k_B T}$, we determine the energy difference between the Fermi level (E_F) and the conduction band edge (E_C), $E_C - E_F \sim 89$ meV, consistent with previous scanning tunneling spectroscopy measurements.[12] From the Hall magnetoresistance, we determine the free electronic carrier density per layer, $n_{2D} = 6.2 \times 10^{10}$ cm^{-2} (Figure 1D). After an *in situ* current annealing procedure, which consists of passing high bias currents through the flake (Figure S2), we observe a decrease in the sample resistance by 2−3 orders of magnitude (Figure 1C) and an increase in the carrier density by 4−5 orders of magnitude to $n_{2D} = 7.4 \times 10^{15}$ cm^{-2} (Figure 1D). The flakes subsequently exhibit metallic behavior and a superconducting transition below ~8 K (Figure 1C).

Figure 2A shows a detailed measurement of the superconducting transition under varying temperature and magnetic field. At zero magnetic field, we identify three distinct regimes. At high temperature, the system appears metallic with only a weak decrease in resistance with decreasing temperature. At ~7.4 K, there is an abrupt kink in the slope of the resistance, and the resistance drops more rapidly with decreasing temperature. At ~2.6 K, there appears a second kink below which the resistance drops quickly to zero within our noise limit. We interpret the two kinks in the temperature dependence as resulting from two distinct superconducting transitions, similar to SNS array systems,[30,31] which we label T_C^{High} and T_C^{Low}, defined as 99% and 10% of the normal state resistance, respectively. Both T_C^{High} and T_C^{Low} shift to lower temperature values with increasing magnetic field (perpendicular to the cluster planes).[32] Below T_C^{Low}, the resistance is thermally activated at a finite magnetic field and well fit by the Arrhenius equation $R = R_0 e^{-U(B)/k_B T}$, where $U(B)$ is the magnetic-field-dependent activation energy, k_B is the Boltzmann constant, and T is the electron temperature (Figure S9).[33] In the intermediate regime between T_C^{High} and T_C^{Low}, the resistance decreases approximately linearly with decreasing temperature. We have measured eight devices fabricated in a similar way, and in all cases we observed superconducting behavior after current annealing (Figure 2C). We note that while we universally observe two superconducting transitions

https://dx.doi.org/10.1021/acs.nanolett.9b04891
Nano Lett. 2020, 20, 1718−1724

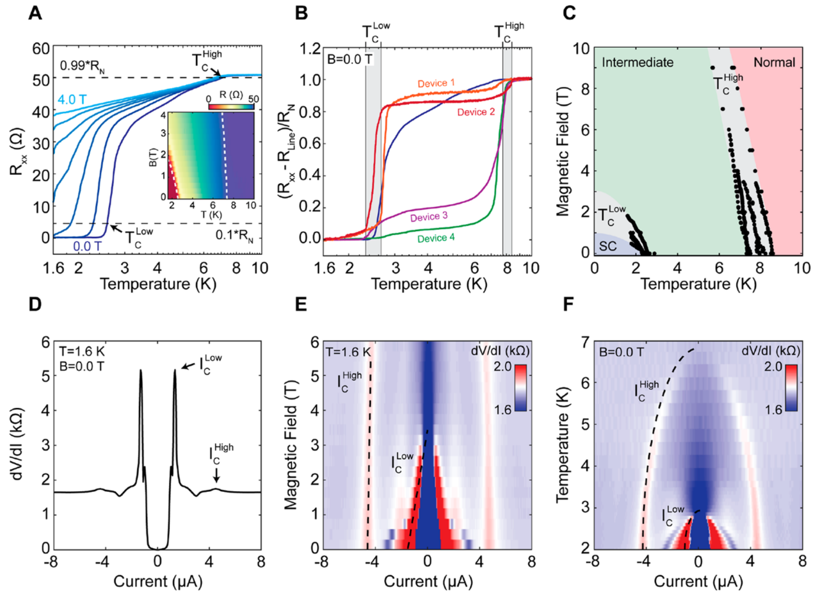

Figure 2. Superconductivity in current annealed $Re_6Se_8Cl_2$. (A) R_{xx} versus temperature of annealed $Re_6Se_8Cl_2$ measured at various magnetic fields. Two transition temperatures ($T_C^{High} \equiv 0.99 \times R_N$) and ($T_C^{Low} \equiv 0.1 \times R_N$) are denoted. Inset: two-dimensional contour plot of R_{xx} versus temperature and magnetic field. Dashed white lines track $0.1 \times R_N$ and $0.99 \times R_N$. (B) R_{xx} versus temperature at zero magnetic field for four additional devices. Each curve has a background resistance subtracted and then is normalized to the normal state resistance. The gray regions represent the ranges of T_C^{High} and T_C^{Low}. The blue curve is the zero field R_{xx} versus temperature for the device in (A). (C) Full magnetic field-temperature phase diagram with T_C^{High} and T_C^{Low} contour lines for eight different $Re_6Se_8Cl_2$ flakes. Normal, superconducting, and intermediate regimes are denoted by red, blue, and green regions, respectively. (D) Differential resistance $R_{xx}^{AC} = \frac{dV}{dI}\Big|_{I_{DC}}$ versus DC current at 1.6 K and zero magnetic field. Two critical currents are denoted I_C^{High} and I_C^{Low}. (E) Two-dimensional contour plot of R_{xx}^{AC} versus DC current and magnetic field. The dashed black lines are a guide to the eye tracking I_C^{High} and I_C^{Low}. (F) Two-dimensional contour plot of R_{xx}^{AC} versus DC current and temperature. The dashed black lines are a guide to the eye tracking I_C^{High} and I_C^{Low}. For (D−F), a background resistance of 156 Ω was subtracted.

with similar values of T_C^{Low} and T_C^{High} the temperature dependence in the transition region between the two superconducting transitions is sample dependent, which we interpret as a result of variability in sample inhomogeneity (Figure 2B and Figure S6).

A full map of the field-temperature phase diagram is shown in the inset of Figure 2A. The critical magnetic field versus temperature is well fit by the relation $H_{C2} = H_{C2-0}\left(1 - \left(\frac{T}{T_C}\right)^2\right)$ for both transitions, where H_{C2} is determined from the $0.1 \times R_N$ and $0.99 \times R_N$ contours, T_C is the corresponding zero-field critical temperature and H_{C2-0} is the zero-temperature upper critical field.[32] From these fits, we determine $H_{C2-0}^{Low} = 3.1$ *T*, and $H_{C2-0}^{High} \approx 32.3$ *T*. Negligible anisotropy is observed in the zero-temperature upper critical field (see Figure S8). Close to T_C, the critical field follows a linear relation, $H_{C2} = \frac{\phi_0}{2\pi\zeta_0^2}\left(1 - \frac{T}{T_C}\right)$ which we use to extract zero-temperature Ginzburg−Landau coherence lengths[32] of $\zeta_0^{Low} = 10.3$ nm and $\zeta_0^{High} = 3.2$ nm. Figure 2C shows an aggregate phase diagram of all measured devices confirming that the equilibrium thermodynamic properties are consistent across all samples (see also Figure S7).

To verify T_C^{High} and T_C^{Low} are consistent with superconducting transitions, we investigate the nonequilibrium properties of an annealed $Re_6Se_8Cl_2$ device by performing critical current measurements (Figure 2D−F).[34,35] Figure 2D presents $R_{AC}(I_{DC}) = \frac{dV}{dI}\Big|_{I_{DC}}$ versus DC current at 1.6 K and zero magnetic field, in which we observe two distinct peak features indicating two critical current values, $I_C^{Low} \sim 1.4$ μA and $I_C^{High} \sim 4.5$ μA. The magnetic field and temperature dependence of I_C^{Low} and I_C^{High} is shown in Figure 2E,F. The extracted thermodynamic quantities from the magnetic field and temperature dependencies,[36] $T_C^{Low} = 2.9$ K, $H_{C2-0}^{Low} = 3.4$ T, and $T_C^{High} = 7.0$ K, $H_{C2-0}^{High} \approx 23.5$ T (Figure S10) are in good agreement with the equilibrium results, confirming that I_C^{Low} and I_C^{High} correspond to the two transitions, T_C^{Low} and T_C^{High}.

We attribute the changes in transport properties after current annealing to a loss of interplanar Cl atoms, as such vacancies have been shown to introduce midgap electronic states resulting in n-type doping.[4,12] The existence of two identifiable superconducting transitions in all samples suggests the existence of two distinct superconducting phases. The key result is the upper transition (T_C^{High}), which we associate with Re_6Se_8 clusters doped from Cl dissociation. The remarkably large upper critical field is comparable to other well-known superconducting 3D Chevrel phase compounds,[20,23−26] which often manifest large upper critical fields as a result of their coherence length via $\left(H_{C2} \propto \frac{1}{\zeta_0^2}\right)$. Chevrel phase superconductors are found to be in the dirty limit in which the coherence length is limited by the mean free path.[20,23,24] The extracted coherence length from our measured upper critical field is $\zeta_0^{High} = 3.2$ nm, similar to the Chevrel phase compounds. The lower superconducting transition (T_C^{Low}) could be a manifestation of superconducting island behavior as a result of the sample inhomogeneity[30,31] or possibly due to a formation of metallic Re[37] from cluster decomposition. While we cannot discount the latter hypothesis, we note that our structural and chemical analyses did not detect the presence of

https://dx.doi.org/10.1021/acs.nanolett.9b04891
Nano Lett. 2020, 20, 1718−1724

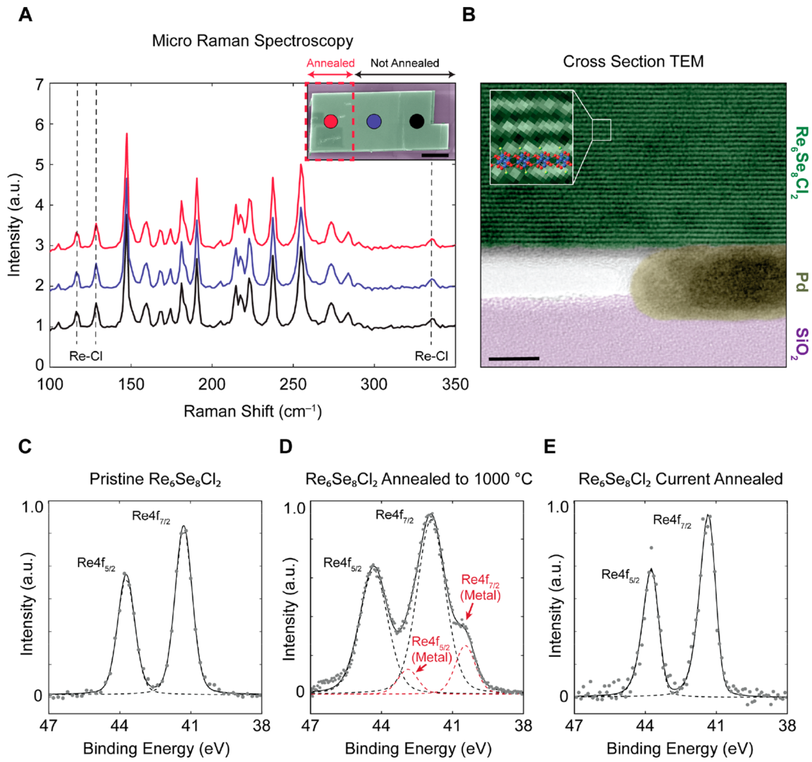

Figure 3. Structural and chemical analyses of annealed $Re_6Se_8Cl_2$. (A) Microscopic Raman spectroscopy of $Re_6Se_8Cl_2$ after current annealing. The spectra are normalized to the intensity at 350 cm^{-1}, then offset from one another by +1. The color of each individual spectrum corresponds to a region in the inset. Inset: SEM image of a flipped $Re_6Se_8Cl_2$ flake after current annealing. The scale bar is 5 μm. The image is false colored so $Re_6Se_8Cl_2$ and SiO_2 appear green and purple, respectively. The colored circles mark the positions where Raman spectroscopy was acquired. The current annealed region is denoted by the red dashed box. (B) Cross-sectional TEM image of a current annealed flake. The scale bar is 10 nm. The image is false colored so $Re_6Se_8Cl_2$, SiO_2, and Pd are green, purple, and yellow, respectively. Inset: enlarged section of the TEM image identifying the Re_6Se_8 cluster planes. (C) μ-XPS Re 4f spectra of pristine microcrystalline $Re_6Se_8Cl_2$. (D) XPS Re 4f spectra of microcrystalline $Re_6Se_8Cl_2$ thermally annealed at 1000 °C. (E) Re 4f μ-XPS spectrum on the current annealed $Re_6Se_8Cl_2$ flake shown in (A). For (C–E), the dashed black and red lines represent single Gaussian fits to the data. Solid black lines are the total fit.

metallic Re in the samples and the upper critical field for the observed transition, H_{C2-0}^{Low}, is ~50 times larger than metallic Re.[37]

To support our proposed doping mechanism through Cl dissociation and better understand the effects of current annealing, we examine the structure and composition of current annealed flakes exhibiting superconducting behavior. Figure 3A presents micro Raman spectra taken on the contact interface of a current annealed flake (see Supporting Information for sample preparation). We measure no deviation in the bulk Raman modes between the current annealed and noncurrent annealed regions.[4] We used focused ion beam (FIB) and transmission electron microscopy (TEM) to obtain a high-resolution cross-sectional image of the device structure after current annealing. We clearly see one of the prepatterned leads and the crystal planes of the Re_6Se_8 cluster layers (Figure 3B). The crystal structure is preserved up to the contact interface.

To measure the chemical state of the annealed material, we performed spatially resolved micro X-ray photoelectron spectroscopy (μ-XPS). We focus specifically on the Re 4f binding energy region to explore the possibility of forming regions of metallic Re during current annealing. As a reference, we performed XPS on $Re_6Se_8Cl_2$, both pristine (Figure 3C) and after thermal annealing at 1000 °C (Figure 3D). The thermal treatment decomposes the surface of the material, and we observe the emergence of two additional peaks corresponding to metallic Re in Figure 3D (see also Figure S15). By comparison, the μ-XPS Re 4f spectrum of the current annealed crystal (Figure 3E) shows no measurable signal from metallic Re. These combined structural and chemical analyses on current annealed flakes suggest the Re_6Se_8 clusters are preserved and any metallic Re resulting from cluster degradation is not detectable by the reported probes.

The exact mechanism responsible for doping of the $Re_6Se_8Cl_2$ crystals remains an open question. Our hypothesis is that localized heating during the current annealing process leads to the dissociation of Cl from the sheets. To support this, we performed three-dimensional steady-state simulations of the heat transfer process using ANSYS Workbench (see Supporting Information for details). Our simulations suggest the temperature can exceed the Cl dissociation temperature (Figure 4) with a strongly localized spatial dependence.

If Cl dissociation does indeed occur due to localized heating, we expect the behavior to be reproducible through a purely thermal process. To understand the relationship between annealing temperature, elemental composition, and electrical properties, we subjected $Re_6Se_8Cl_2$ to a series of heat treatments and characterized the resulting samples. For these experiments, the material is sealed in fused silica tubes under vacuum and annealed at set temperatures up to 1000 °C. We use XPS and energy dispersive X-ray (EDX) spectroscopy to determine the surface and bulk elemental compositions, respectively. When the material is heated to 400 °C, XPS

https://dx.doi.org/10.1021/acs.nanolett.9b04891
Nano Lett. 2020, 20, 1718–1724

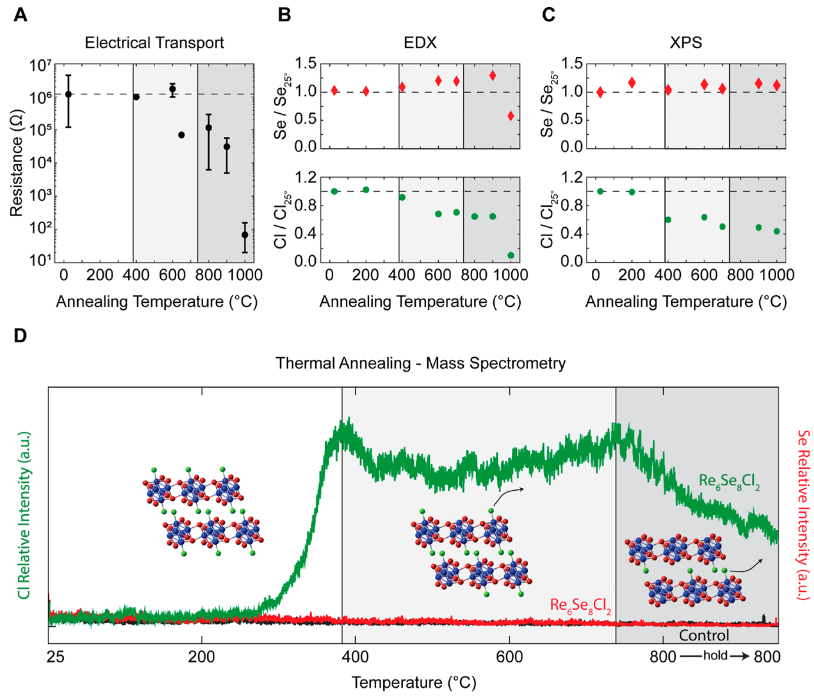

Figure 4. Chemical analysis of thermally annealed $Re_6Se_8Cl_2$. (A) Two-terminal resistance of bulk single crystal $Re_6Se_8Cl_2$ versus annealing temperature. Resistance was measured in the linear IV regime. (B) Relative Se and Cl loss measured by EDX versus annealing temperature. Values for each element were calculated by dividing the measured atomic percentage at each temperature by the atomic percentage of the nonannealed sample (25 °C). (C) Relative Se and Cl loss measured by XPS versus annealing temperature. Values were calculated by dividing each element's integrated spectrum area by the Re 4f spectrum area for each temperature then dividing each ratio by the nonannealed ratio (25 °C). (D) Cl_2^- and Cl^- mass counts versus time as $Re_6Se_8Cl_2$ powder (green) and an empty crucible (black) are heated from 25 to 800 °C. The red line is a measurement of Se^-, Se_2^-, and Se_3^- counts for the $Re_6Se_8Cl_2$ powder. In (A–D), the white, light gray, and dark gray regions correspond to no loss of Cl, a loss of surface Cl, and a loss of bulk Cl, respectively. A schematic of the proposed dissociation process is shown for each region in (D).

reveals a decrease in the surface Cl concentration when compared to the pristine material (Figure 4C), whereas EDX only shows a slight decrease in the bulk Cl signal. Between 400 and 600 °C, the bulk Cl concentration shows a dramatic decrease (Figure 4B), which coincides with a decrease in the resistance of the material by 1−2 orders of magnitude (Figure 4A). When $Re_6Se_8Cl_2$ is annealed to 1000 °C, we observe a further decrease of the bulk Cl elemental composition by EDX, as well as a loss of Se, indicating an onset of cluster decomposition. We note that single crystal X-ray diffraction indicates that the bulk crystal structure is unchanged across the whole temperature range (Figure S14).

Our observations of Cl loss are corroborated by performing real time thermal annealing-mass spectrometry (TA-MS) analysis (see Supporting Information for details). Figure 4D shows the combined intensity responses for the Cl^- and Cl_2^- ions when $Re_6Se_8Cl_2$ (green) and a control empty crucible (black) are gradually heated from 25 to 800 °C, while the red trace measures the combined Se^-, Se_2^-, and Se_3^- signals. The Cl signal shows two peaks at ∼385 and ∼763 °C, suggesting the onset of two different Cl dissociation processes. The higher temperature peak agrees with the bulk Cl loss temperature while the lower temperature peak may be attributed to the dissociation of surface level Cl atoms. We also note that no Se signal is observed up to 800 °C. Taken together, these results demonstrate that the Cl dissociation and doping process can be thermally driven and occur without a loss of the intrinsic Re_6Se_8 cluster structure.

The bulk thermal annealing results, in combination with the thermal modeling and the chemical and structural analysis on current annealed flakes, suggest that the current annealing procedure results in electron doping through Cl dissociation as a result of sample heating. Although thermal annealing has not reproduced the same signatures of superconductivity, future work will focus on exploring the vast thermal annealing phase space to produce bulk Re_6Se_8 cluster superconductivity.

We have reported the first observation of superconductivity in a vdW superatomic crystal. Through both current and thermal annealing processes, we demonstrate that $Re_6Se_8Cl_2$ can lose interplanar Cl atoms, while retaining the integrity of the Re_6Se_8 clusters. This leads to a dramatic increase in carrier concentration and gives rise to clear signatures of robust Re_6Se_8 cluster superconductivity. These results offer the possibility of generalizing this approach to electronically dope other vdW materials with labile halide ligands. We envision using the annealing process to write metallic or superconducting patterns on the nanoscale, using techniques such as atomic force microscopy and scanning tunneling spectroscopy to controllably dope well-defined regions.

■ ASSOCIATED CONTENT

Supporting Information

The Supporting Information is available free of charge at https://pubs.acs.org/doi/10.1021/acs.nanolett.9b04891.

Synthesis, device fabrication, transport measurements, current annealing, modeling details, superconducting properties, chemical and structural analysis details, Supporting Figures S1−S18, Table S1 (PDF)

https://dx.doi.org/10.1021/acs.nanolett.9b04891
Nano Lett. 2020, 20, 1718−1724

AUTHOR INFORMATION

Corresponding Authors

Xavier Roy – *Department of Chemistry, Columbia University, New York, New York 10027, United States;* orcid.org/0000-0002-8850-0725; Email: xr2114@columbia.edu

Cory R. Dean – *Department of Physics, Columbia University, New York, New York 10027, United States*; Email: cd2478@columbia.edu

Authors

Evan J. Telford – *Department of Physics, Columbia University, New York, New York 10027, United States;* orcid.org/0000-0002-9494-9166

Jake C. Russell – *Department of Chemistry, Columbia University, New York, New York 10027, United States*

Joshua R. Swann – *Department of Physics, Columbia University, New York, New York 10027, United States*

Brandon Fowler – *Department of Chemistry, Columbia University, New York, New York 10027, United States*

Xiaoman Wang – *Department of Mechanical Engineering, Carnegie Mellon University, Pittsburgh, Pennsylvania 15213, United States*

Kihong Lee – *Department of Chemistry, Columbia University, New York, New York 10027, United States*

Amirali Zangiabadi – *Department of Applied Physics and Applied Mathematics, Columbia University, New York, New York 10027, United States*

Kenji Watanabe – *National Institute for Materials Science, Tsukuba 305-0044, Japan;* orcid.org/0000-0003-3701-8119

Takashi Taniguchi – *National Institute for Materials Science, Tsukuba 305-0044, Japan;* orcid.org/0000-0002-1467-3105

Colin Nuckolls – *Department of Chemistry, Columbia University, New York, New York 10027, United States;* orcid.org/0000-0002-0384-5493

Patrick Batail – *Department of Chemistry, Columbia University, New York, New York 10027, United States; Laboratoire MOLTECH, CNRS UMR 6200, Université d'Angers, 49045 Angers, France;* orcid.org/0000-0001-7125-5009

Xiaoyang Zhu – *Department of Chemistry, Columbia University, New York, New York 10027, United States;* orcid.org/0000-0002-2090-8484

Jonathan A. Malen – *Department of Mechanical Engineering, Carnegie Mellon University, Pittsburgh, Pennsylvania 15213, United States;* orcid.org/0000-0003-4560-4476

Complete contact information is available at:
https://pubs.acs.org/10.1021/acs.nanolett.9b04891

Author Contributions

The manuscript was written through contributions of all authors. All authors have given approval to the final version of the manuscript.

Author Contributions

[∇]E.J.T. and J.C.R. contributed equally.

Notes

The authors declare no competing financial interest.

ACKNOWLEDGMENTS

We thank Abhay Pasupathy, James Hone, and Avishai Benyamini for fruitful discussions and input. We also thank Dan Paley for assistance with the SCXRD and XPS measurements and Tai-De Li for assistance with the micro XPS. Sample preparation and transport measurements were primarily supported by the NSF MRSEC program through the Center for Precision Assembly of Superstratic and Superatomic Solids (DMR-1420634). Chemical and structural analyses (XPS, TA-MS, SCXRD, TEM) were supported by the NSF CAREER award (DMR-1751949). Raman spectroscopy was supported by the U.S. Air Force Office of Scientific Research (AFOSR) Grant FA9550-18-1-0020. Thermal transport modeling was supported by the Army Research Office Grant W911NF1710397. J.C.R. is supported by the U.S. Department of Defense through the National Defense Science and Engineering Graduate Fellowship (NDSEG) Program.

ABBREVIATIONS

vdW, van der Waals; BN, boron nitride; TMD, transition metal dichalcogenide; FIB, focused ion beam; TEM, transmission electron microscopy; μ-XPS, micro X-ray photoelectron spectroscopy; EDX, energy dispersive X-ray spectroscopy; TA-MS, thermal annealing-mass spectrometry

REFERENCES

(1) Pinkard, A.; Champsaur, A. M.; Roy, X. Molecular Clusters: Nanoscale Building Blocks for Solid-State Materials. *Acc. Chem. Res.* **2018**, *51* (4), 919–929.

(2) Hernández Sánchez, R.; Champsaur, A. M.; Choi, B.; Wang, S. G.; Bu, W.; Roy, X.; Chen, Y. S.; Steigerwald, M. L.; Nuckolls, C.; Paley, D. W. Electron Cartography in Clusters. *Angew. Chem., Int. Ed.* **2018**, *57* (42), 13815–13820.

(3) Roy, X.; Lee, C. H.; Crowther, A. C.; Schenck, C. L.; Besara, T.; Lalancette, R. A.; Siegrist, T.; Stephens, P. W.; Brus, L. E.; Kim, P.; et al. Nanoscale Atoms in Solid-State Chemistry. *Science* **2013**, *341* (6142), 157–160.

(4) Choi, B.; Lee, K.; Voevodin, A.; Wang, J.; Steigerwald, M. L.; Batail, P.; Zhu, X.; Roy, X. Two-Dimensional Hierarchical Semiconductor with Addressable Surfaces. *J. Am. Chem. Soc.* **2018**, *140* (30), 9369–9373.

(5) Champsaur, A. M.; Velian, A.; Paley, D. W.; Choi, B.; Roy, X.; Steigerwald, M. L.; Nuckolls, C. Building Diatomic and Triatomic Superatom Molecules. *Nano Lett.* **2016**, *16* (8), 5273–5277.

(6) O'Brien, E. S.; Trinh, M. T.; Kann, R. L.; Chen, J.; Elbaz, G. A.; Masurkar, A.; Atallah, T. L.; Paley, M. V.; Patel, N.; Paley, D. W.; et al. Single-Crystal-to-Single-Crystal Intercalation of a Low-Bandgap Superatomic Crystal. *Nat. Chem.* **2017**, *9* (12), 1170–1174.

(7) Ong, W. L.; O'Brien, E. S.; Dougherty, P. S. M.; Paley, D. W.; Fred Higgs, C.; McGaughey, A. J. H.; Malen, J. A.; Roy, X. Orientational Order Controls Crystalline and Amorphous Thermal Transport in Superatomic Crystals. *Nat. Mater.* **2017**, *16* (1), 83–88.

(8) Lee, K.; Choi, B.; Plante, I. J.-L.; Paley, M. V.; Zhong, X.; Crowther, A. C.; Owen, J. S.; Zhu, X.; Roy, X. Two-Dimensional Fullerene Assembly from an Exfoliated van Der Waals Template. *Angew. Chem., Int. Ed.* **2018**, *57* (21), 6125–6129.

(9) Reber, A. C.; Khanna, S. N. Superatoms: Electronic and Geometric Effects on Reactivity. *Acc. Chem. Res.* **2017**, *50* (2), 255–263.

(10) Lee, C.-H.; Liu, L.; Bejger, C.; Turkiewicz, A.; Goko, T.; Arguello, C. J.; Frandsen, B. A.; Cheung, S. C.; Medina, T.; Munsie, T. J. S.; et al. Ferromagnetic Ordering in Superatomic Solids. *J. Am. Chem. Soc.* **2014**, *136* (48), 16926–16931.

(11) Allemand, P.-M.; Khemani, K. C.; Koch, A.; Wudl, F.; Holczer, K.; Donovan, S.; Gruner, G.; Thompson, J. D. Organic Molecular Soft Ferromagnetism in a Fullerene C60. *Science* **1991**, *253* (5017), 301–302.

(12) Zhong, X.; Lee, K.; Choi, B.; Meggiolaro, D.; Liu, F.; Nuckolls, C.; Pasupathy, A.; De Angelis, F.; Batail, P. R.; Roy, X.; et al. Superatomic Two-Dimensional Semiconductor. *Nano Lett.* **2018**, *18*, 1483–1488.

(13) Lee, K.; Maehrlein, S. F.; Zhong, X.; Meggiolaro, D.; Russell, J. C.; Reed, D. A.; Choi, B.; De Angelis, F.; Roy, X.; Zhu, X. Hierarchical Coherent Phonons in a Superatomic Semiconductor. *Adv. Mater.* **2019**, *31*, 1903209.
(14) Zhong, X.; Lee, K.; Meggiolaro, D.; Dismukes, A. H.; Choi, B.; Wang, F.; Nuckolls, C.; Paley, D. W.; Batail, P.; De Angelis, F.; et al. Mo6S3Br6: An Anisotropic 2D Superatomic Semiconductor. *Adv. Funct. Mater.* **2019**, *29*, 1902951.
(15) Novoselov, K. S.; Mishchenko, A.; Carvalho, A.; Neto, A. H. C. 2D Materials and van Der Waals Heterostructures. *Science* **2016**, *353* (6298), aac9439.
(16) Coleman, J. N.; Khan, U.; Young, K.; Gaucher, A.; De, S.; Smith, R. J.; Shvets, I. V.; Arora, S. K.; Stanton, G.; Kim, H.; et al. Two-Dimensional Nanosheets Produced by Liquid Exfoliation of Layered. *Science* **2011**, *331* (6067), 568−571.
(17) Choi, B.; Yu, J.; Paley, D. W.; Trinh, M. T.; Paley, M. V.; Karch, J. M.; Crowther, A. C.; Lee, C. H.; Lalancette, R. A.; Zhu, X.; et al. Van Der Waals Solids from Self-Assembled Nanoscale Building Blocks. *Nano Lett.* **2016**, *16* (2), 1445−1449.
(18) Leduc, L.; Perrin, A.; Sergent, M. Structure Du Dichlorure et Oetaseleniure d'Hexarhenium, Re6Se8Cl2: Compose Bidimensionnel a Clusters Octaedriques Re6. *Acta Crystallogr., Sect. C: Cryst. Struct. Commun.* **1983**, *39*, 1503−1506.
(19) Burdett, J. K.; Lin, J. H. The Structures of Chevrel Phases. *Inorg. Chem.* **1982**, *21* (1), 5−10.
(20) Peña, O. Chevrel Phases: Past, Present and Future. *Phys. C* **2015**, *514*, 95−112.
(21) Gabriel, J. C. P.; Boubekeur, K.; Uriel, S.; Batail, P. Chemistry of Hexanuclear Rhenium Chalcohalide Clusters. *Chem. Rev.* **2001**, *101*, 2037−2066.
(22) Leduc, L.; Padiou, J.; Perrin, A.; Sergent, M. Synthese et Caracterisation d'un Nouveau Chalcohalogenure a Clusters Octahedriques de Rhenium a Caractere Bidimensionnel: Re6Se8Cl2. *J. Less-Common Met.* **1983**, *95*, 73−80.
(23) Chen, J.; Millis, A. J.; Reichman, D. R. Intermolecular Coupling and Superconductivity in $PbMo_6S_8$ and Other Chevrel Phase Compounds. *Phys. Rev. Mater.* **2018**, *2* (11), 114801.
(24) Fischer, Ø. Chevrel Phases: Superconducting and Normal State Properties. *Appl. Phys.* **1978**, *16* (1), 1−28.
(25) Xie, W.; Luo, H.; Phelan, B. F.; Klimczuk, T.; Cevallos, F. A.; Cava, R. J. Endohedral Gallide Cluster Superconductors and Superconductivity in $ReGa_5$. *Proc. Natl. Acad. Sci. U. S. A.* **2015**, *112* (51), E7048−E7054.
(26) Ganin, A. Y.; Takabayashi, Y.; Jeglič, P.; Arčon, D.; Potočnik, A.; Baker, P. J.; Ohishi, Y.; McDonald, M. T.; Tzirakis, M. D.; McLennan, A.; et al. Polymorphism Control of Superconductivity and Magnetism in Cs_3C_{60} Close to the Mott Transition. *Nature* **2010**, *466* (7303), 221−225.
(27) Wang, H.; Huang, X.; Lin, J.; Cui, J.; Chen, Y.; Zhu, C.; Liu, F.; Zeng, Q.; Zhou, J.; Yu, P.; et al. High-Quality Monolayer Superconductor $NbSe_2$ Grown by Chemical Vapour Deposition. *Nat. Commun.* **2017**, *8* (1), 394.
(28) Qi, Y.; Naumov, P. G.; Ali, M. N.; Rajamathi, C. R.; Schnelle, W.; Barkalov, O.; Hanfland, M.; Wu, S. C.; Shekhar, C.; Sun, Y.; et al. Superconductivity in Weyl Semimetal Candidate $MoTe_2$. *Nat. Commun.* **2016**, *7*, 11038.
(29) Yankowitz, M.; Chen, S.; Polshyn, H.; Zhang, Y.; Watanabe, K.; Taniguchi, T.; Graf, D.; Young, A. F.; Dean, C. R. Tuning Superconductivity in Twisted Bilayer Graphene. *Science* **2019**, *363* (6431), 1059−1064.
(30) Eley, S.; Gopalakrishnan, S.; Goldbart, P. M.; Mason, N. Approaching Zero-Temperature Metallic States in Mesoscopic Superconductor−Normal−Superconductor Arrays. *Nat. Phys.* **2012**, *8* (1), 59−62.
(31) Sun, Y.; Xiao, H.; Zhang, M.; Xue, Z.; Mei, Y.; Xie, X.; Hu, T.; Di, Z.; Wang, X. Double Quantum Criticality in Superconducting Tin Arrays-Graphene Hybrid. *Nat. Commun.* **2018**, *9* (1), 2159.
(32) Tinkham, M. *Introduction to Superconductivity*, 2nd ed.; Dover Publ: Mineola, NY, 2004.
(33) Feigel'man, M. V.; Geshkenbein, V. B.; Larkin, A. I. Pinning and Creep in Layered Superconductors. *Phys. C* **1990**, *167* (1−2), 177−187.
(34) Ueno, K.; Nakamura, S.; Shimotani, H.; Ohtomo, A.; Kimura, N.; Nojima, T.; Aoki, H.; Iwasa, Y.; Kawasaki, M. Electric-Field-Induced Superconductivity in an Insulator. *Nat. Mater.* **2008**, *7* (11), 855−858.
(35) Ueno, K.; Nakamura, S.; Shimotani, H.; Yuan, H. T.; Kimura, N.; Nojima, T.; Aoki, H.; Iwasa, Y.; Kawasaki, M. Discovery of Superconductivity in KTaO3 by Electrostatic Carrier Doping. *Nat. Nanotechnol.* **2011**, *6*, 408−412.
(36) Dew-Hughes, D. The Critical Current of Superconductors: An Historical Review. *Low Temp. Phys.* **2001**, *27*, 713−722.
(37) Daunt, J. G.; Smith, T. S. Superconductivity of Rhenium. *Phys. Rev.* **1952**, *88* (2), 309−311.

https://dx.doi.org/10.1021/acs.nanolett.9b04891
Nano Lett. 2020, 20, 1718−1724